Received: 4 September 2023 | Revised: 4 February 2024 | Accepted: 27 February 2024 | Published online: 4 March 2024

RESEARCH ARTICLE

Medinformatics
2024, Vol. 1(2) 79–90
DOI: 10.47852/bonviewMEDIN42021685

BON VIEW PUBLISHING

Proportion Estimation and Multi-Class Classification of Abnormal Brain Cells

Meenal Joshi[1,*] and Bhupesh Kumar Singh[1]

[1]*Department of Computer Engineering, G. B. Pant University of Agriculture and Technology, India*

Abstract: Vagueness in the determination of the tumor size creates significant hindrances in planning and quantitatively assessing brain tumor (BT) treatments. Non-invasive magnetic resonance imaging (MRI) has become a primary non-ionizing radiation diagnostic tool for brain cancers. It takes a long time to manually segment the extent of a BT from 3D MRI volumes, and the performance heavily depends on the operator's skill. A precise and automated BT segmentation tool is needed desperately. In this case, an accurate assessment of the tumor's extent requires a reliable automated segmentation method for the BT. The multimodal BT image segmentation (BRATS 2020) dataset is used in this paper to demonstrate an automated deep convolutional network, or U-Net, method for BT segmentation. Deep learning and transfer learning are utilized to improve the accuracy and effectiveness in detecting and recognizing different types of brain cancers. The unobserved images' F1 scores were 98% and 99%, respectively.

Keywords: BRATS, convolutional neural network, ResNet, segmentation, U-Net

1. Introduction

The human brain is a most vital organ. The body's sensory organs provide impulses or signals to the brain, which processes them, makes the final decision, and actuates through the muscles. Brain tumor (BT) is nemesis of the human brain. It is an uncontrolled growth of abnormal brain cells [1]. The two main categories of BTs are primary and metastatic (secondary).

Primary BTs comprise human cells and are often benign. In contrast, blood flow from other body areas helped metastatic cancers reach the brain.

Metastatic tumors are the terrifying one, because of the lousy prognosis as well as the immediate effects on the quality of life and diminished cognitive functions. Gliomas and primary central nervous system lymphomas, accounting for about 80% of malignant cases, are adults' most common primary BTs [2]. A 2.5-year cumulative relative survival rate of 2% and 8% at 10 years for metastasis and high-grade glioblastoma, respectively, is still regarded as untreatable despite significant advancements in chemotherapy, radiation, imaging, and surgical technique [3]. Additionally, the prognosis for individuals with low-grade gliomas varies, with a 10-year survival rate generally of around 57% [4]. A general categorization of such malignant cells is given in Table 1.

This has been reported that the features of newly discovered BTs on magnetic resonance imaging (MRI) can be utilized to predict the likely diagnosis and course of therapy [5–7]. Additionally, multimodal MRI procedures are typically employed to assess BTs' blood–brain barrier integrity, cellularity, and vascularity. This is so that the various image contrasts produced by multimodal MRI techniques may provide essential complementary information. T2, T1-weighted (with FLAIR, or fluid-attenuated inversion recovery), and gadolinium-enhanced T1-weighted imaging sequences are examples of common BT MRI procedures that are often utilized. These structural MRI scans usually provide a useful diagnostic [8].

The process of using MRI images for BT studies requires image segmentation for two reasons: (1) the segmented BT extent can remove distracting structures from other brain tissues, which leads to a more accurate classification for the subtypes of BTs and helps with the subsequent diagnosis and (2) the precise delineation is critical for radiotherapy or surgical planning, as it provides information on both the BT and surrounding healthy tissue. Currently, segmentation in clinical practice is still done manually by human operators using demarcation. Manual segmentation is a labor-intensive process that frequently uses slice-by-slice techniques, and the results rely heavily on the experience and subjective opinion of the operators. Furthermore, repeatable results are challenging for even the same operator to produce. There is a strong demand for a completely automated, objective, and reproducible segmentation approach for a longitudinal, multimodal, and multi-institutional clinical study.

The brain lesions vary greatly in their location, shape, appearance, size, and regularity (such as contrast texture, uptake, and image uniformity), which presents several challenges for BT segmentation even with fully automatic and semi-automated algorithms available [5, 9]. Low signal-to-noise ratios might arise from this, and the accuracy of the final segmentation could also be impacted by asymmetric partial volume effects. In general, methodologies based on supervised learning [9–14] and unsupervised learning [15–17] may be classified as having been applied in earlier research on BT segmentation. Other sources, like Bauer et al. [5], provide a more in-depth thematic assessment

*Corresponding author: Meenal Joshi, Department of Computer Engineering, G. B. Pant University of Agriculture and Technology, India. Email: 58409_meenaljoshi@gbpuat-tech.ac.in

Table 1. Categorization of malignant cells

Type of tumor	Description	Pictorial representation
Glioma	Gliomas are a kind of tumor that can grow in the brain or spinal cord. Gliomas start in the adherent support cells that envelop and facilitate the function of nerve cells. Gliomas are classified according to their hereditary topographies and the percentage of glial cells in the tumor. This can help forecast how the tumor will behave and potential treatment approaches. A glioma tumor may present as imbalance, annoyance, nausea, a decrease in brain function, or a misperception	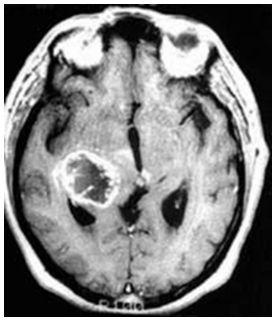
Meningioma	A meningioma is a kind of tumor that encircles the meninges, brain, or spinal cord. It is not a brain tumor per se, but it fits the description since it can compress nearby blood arteries, nerves, or the brain. The most common kind of tumor that forms in the head is a meningioma. The symptoms of meningioma usually appear gradually, and they may be greatly underestimated at first. The symptoms and signs of cancer can vary depending on whether it is in the brain or, less commonly, the backbone. They can include changes in vision, such as sightedness or vagueness; headaches, hearing problems or buzzing in the ears; memory loss; seizures; and trouble speaking	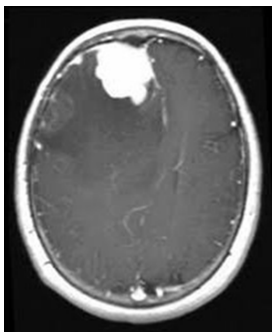
Pituitary	Uncontrollable growths in the pituitary gland are known as pituitary tumors. Hormones that regulate growth and development, organ function (including those of the kidneys, breasts, and uterus), and gland function are produced by some pituitary tumors. The pituitary gland may produce fewer hormones as a result of some pituitary tumors. Adenomas, or benign growths that are not malignant, make up the majority of pituitary tumors Adenomas stay restricted to the pituitary gland or surrounding tissues; they do not spread to other regions of the body	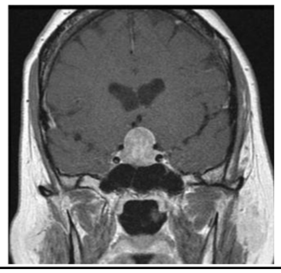

of the various BT segmentation techniques. Additionally, a specialized yearly workshop and competition called multimodal BT image segmentation is performed to compare multiple algorithms created for the segmentation of BTs [18].

2. Materials and Methods

2.1. Computational resources

In the Google Colab environment, the results were obtained with the use of computer resources, namely an i3 CPU and 16 GB of RAM. The method is implemented using PyTorch. The network is trained on an NVIDIA GeForce R.T.X. 2080 Ti GPU and an Intel Core i3 Processor E5-2650 v3 @ 2.30GHz 20, with 16 GB of RAM. We did not use any fresh datasets to prepare our network. For training, we selected photos and scaled them to create non-overlapping patches of size 100 × 100.

Four patches from several parametric images—FLAIR, T1ce, T2, and T1 images—are combined to provide the network's input. We have lesioned the edge impact in segmentation maps using the U-Net model.

2.2. Brain MRI data acquisitions

This investigation used two MRI datasets that were available to the public. The online-available dataset is used as information obtained by medical examiners, including radiologists and doctors. Several research has also examined this dataset. With a primary focus on the segmentation and 3,064 brain MRI slices acquired from 233 patients, respectively, we used a public BT dataset from Brats and a Figshare source comprising BraTS 2020 multi-institutional pre-operative MRI images. Glioma, pituitary, meningioma, and no-tumor pictures are among the four types of BTs involved. Available in ".jpg" format is the dataset. Each jpg file has a structure that includes an image ID, 512 × 512 pixels of unified picture data, the kinds of BTs, the tumor boundary with coordinate points, and ground truth in a binary mask image. The labels of the MRI dataset are displayed in Figure 1(B), with the tumor being shown in one category with the title "Pituitary," "Glioma," or "meningioma," and with no cancer being shown in another with the label "no tumor." ResNet architecture takes the image as input, so our experiment used image data from the .jpg files. Additionally, Table 2 shows the database description for multi-class classification.

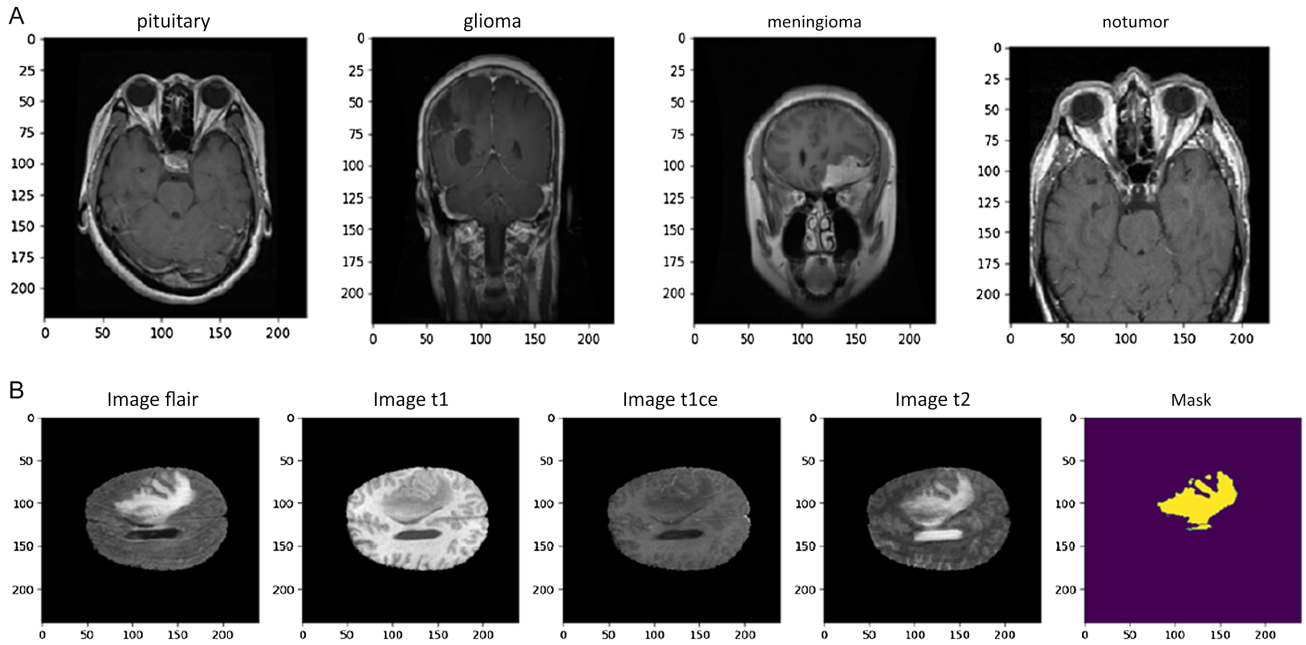

Figure 1. (A) Various MRI tumor scans and (B) brain scans for segmentation

Table 2. Description of the dataset

Category	Number of slices in training	Number of slices in testing
No tumor	1595	405
Pituitary	1457	300
Meningioma	1339	306
Glioma	1321	300
Total	**5712**	**1311**

The BRATS 2020 dataset, which includes four basic categories: "NOT tumor," "NECROTIC/CORE," "EDOEMA," and "ENHANCING" of the patient scans, was used to test and assess the suggested technique. Each patient in the BRATS 2020 datasets has access to multimodal MRI data, and four MRI scanning sequences employing T1-weighted (T1), T1-weighted imaging (T1c), T2-weighted (T2), and FLAIR were carried out for each patient as shown in Figure 1(B). The T2, FLAIR, and T1 images were co-registered into the T1c data, with the highest spatial resolution for each patient. For every multimodal MRI sequence, we used data normalization.

Additionally, for each instance, manual segmentations with the intra-tumoral classifications of edema (1), necrosis (2), enhancing tumor (3), and non -enhancing tumor (4) are accessible. Manual segmentations have been employed as the source of truth for both the segmentation model training and the final segmentation performance evaluation. In earlier investigations, multimodal data were layered like RGB multichannel pictures [19–21]. In this work, we successfully segmented all tumor areas and regions using FLAIR images [9]. Additionally, the enhancing tumor was defined using T1c data. As a result, our methodology is more effective and requires fewer clinical inputs, as patient symptoms and short acquisition times usually prevent the availability of multimodal MRI data. The dataset distribution for tumor proportion estimation is as follows:

- Training slices: 245, validation slices: 87, and testing slices: 48.

2.3. Preprocessing

Since intensity variation encodes all of the information about the brain, the contract must be carefully considered while analyzing or deciphering brain pictures. Thus, preprocessing is necessary to remove unnecessary marks and labels from the image. Preprocessing approaches enhance image quality, eliminate any previously present noise in the image, and set up the idea for later processing [22].

Unlike many other deep learning algorithms that use the entire image, we focused only on a tiny area of the image to extract the fundamental properties. The unfavorable outcomes are greatly lessened by removing these meaningless, uninformative components [23]. A total of 5.38 ms time is taken while preprocessing the brain MRI scans. Table 3 shows the steps involved along with the outcome achieved.

Following are the steps involved in the preprocessing with the outcome image.

2.4. Data augmentation

By purposefully providing extra training data from the original set, data augmentation aims to increase network performance. We used various data augmentation techniques in this research. Simple transformations like flipping, rotating, shifting, and zooming can provide displacement fields for images, but they do not give training examples with significantly altered shapes. Since tumors lack a characteristic form, shear surgery can somewhat affect the general structure of the tumor in a horizontal orientation but still cannot provide sufficiently diverse training data. To address this issue, we also used **Height_Shift_Range = 0.05** and **Width_Shift_Range = 0.05** [24], **Rotation_Range = 10**, and **Horizontal_Flip = True** which may produce additional training data with arbitrary but acceptable forms. Figure 2 shows the augmented output for the given original image as input.

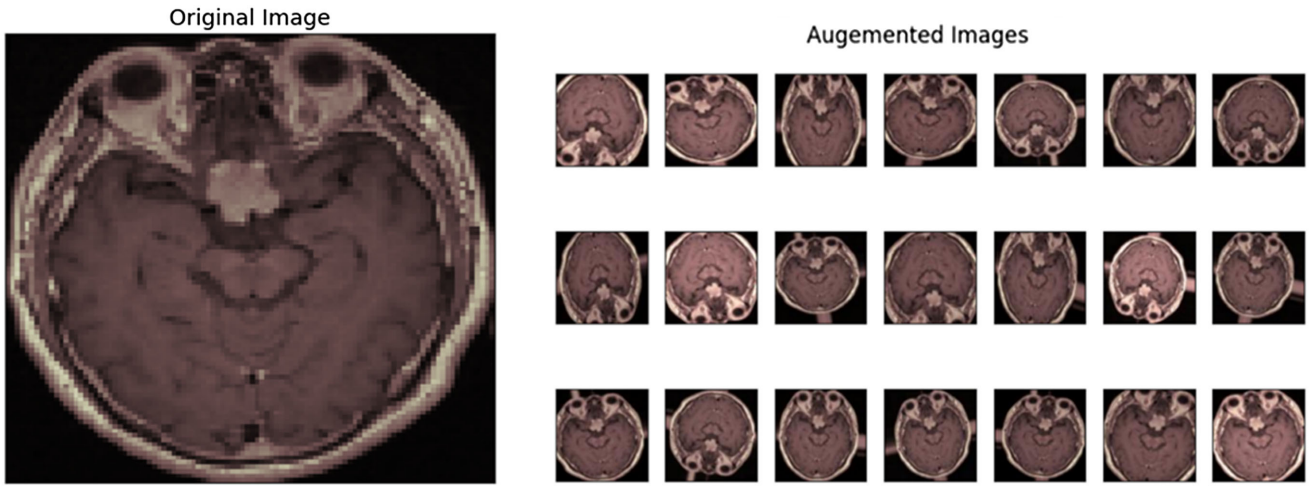

Figure 2. Output obtained after augmentation

2.5. Proposed method for multi-class classification

The suggested approach for this investigation entails multiple steps. These are the phases: image capture with tumor detection. All preprocessed images will be split into validation, testing, and training sets to train in a transfer learning environment and subsequently test using testing data. Preparing images include converting them to grayscale, cropping them to remove as much of the black background as possible, enhancing contrast to obtaining more accurate data, and thresholding to isolate the tumor's specific location. The ResNet model is created after the training procedure. The results will be obtained using this ResNet model as a classification engine.

ResNet trains on $F(X)$, as opposed to all other algorithms, which train on the output $'Y'$. To put it another way, ResNet seeks to make $F(X) = 0$ such that $Y = X$. The suggested model's flow diagram is shown in Figure 3.

2.5.1. ResNet-50

Residual neural networks are artificial neural networks that construct networks using residual blocks. The term ResNet-50 refers to a convolutional neural network (CNN) with 50 layers. The 50-layer CNN is composed of 48 convolutional layers, 1 MaxPool layer, and 1 average pool layer. One MaxPool layer, one average pool layer, and 48 convolutional layers make up the 50-layer CNN. A neural network that serves as the foundation for a number of computer vision applications is known by the general term ResNet, or residual networks. The main innovation of ResNet was its capacity to train incredibly intricate neural networks with over 150 layers. Table 4 depicts the modified parameters used in implementing ResNet-50.

a.Unique features of ResNet-50

The architecture of ResNet-50 is based on the concept shown above, with one significant exception. The bottleneck building block is used in the 50-layer ResNet. A bottleneck residual block uses 11 convolutions to reduce the number of parameters and matrix multiplications and is frequently referred to as a "bottleneck." This greatly accelerates the training of each layer. Instead of using a stack of two levels, it employs three layers.

Table 3. Obtained cropped brain scan

Steps	Outcome
• Obtaining the original image	Step 1. Get the original image 
• Finding the biggest contour	Step 2. Find the biggest contour 
• Finding the extreme points	Step 3. Find the extreme points 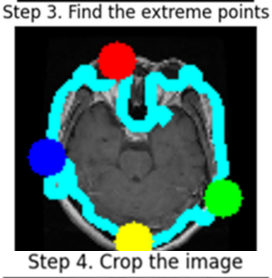
• Obtaining the final image	Step 4. Crop the image 

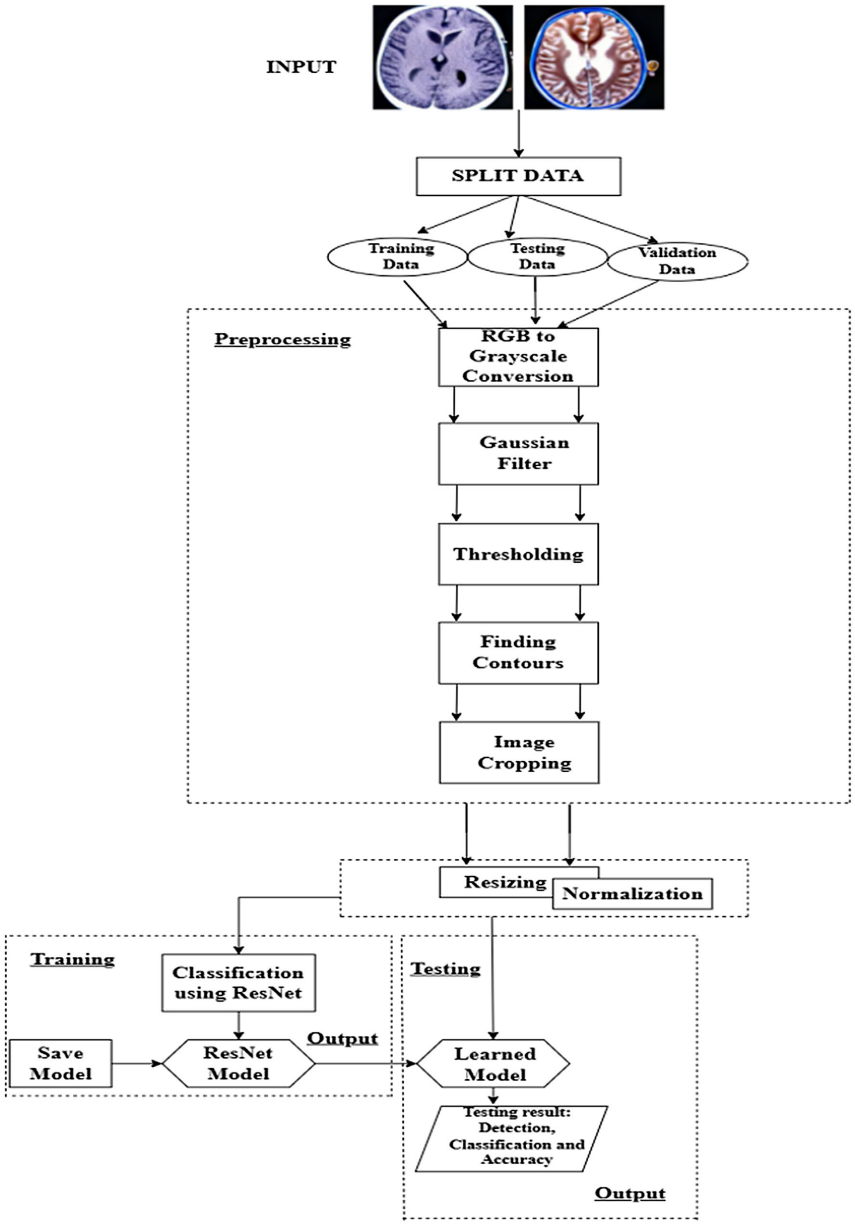

Figure 3. Proposed architecture for brain lesion classification

Table 4. Parameters used in implementation

	ResNet-50 implementation						
Proposed architecture	Convolutional layers	Dropout layers	Activation	Max pooling	Dense layer	Batch normalization	Number of parameters
ResNet-50	48	1	49	1	1	53	23,328,644
			ResNet-101 implementation				
ResNet-101	99	1	99	1	1	106	42,666,372

2.5.2. ResNet-101

ResNet-101 is the name of a CNN that has 101 layers. A pre-trained version of the network, trained on over a million photos, is available in the ImageNet database [1]. The pre-trained network can categorize photos into 1000 different item categories, including several animals, a keyboard, a mouse, and a pencil. As a result, the network now includes rich feature representations for a wide range of pictures. Images having a resolution of 224 by 224 are supported by the network. Table 4 depicts the modified parameters used in implementing ResNet-101.

2.5.3. Hyperparameters

A parameter established before the learning process starts is called a hyperparameter. These adjustable settings have a direct impact on how successfully a model trains. Table 5 describes the hyperparameters used in the proposed approach.

Table 5. List of hyperparameters used in the work

Model	ResNet-50, ResNet-101
Activation	Softmax
Image size	100,100
Weights	Image net
Optimizer	Adam
Dropout	0.2
Metrics	Accuracy
Loss	Categorical cross entropy
Epochs	60
Batch size	28
Learning rate	0.0001
Monitor	Val_loss
Backbone	ResNet-50 and ResNet-101, respectively

2.6. U-Net-based deep CNNs

Biomedical images frequently feature intricate patterns of the photographed item (such as a BT), and the object's edge might vary. To handle the segmentation for the objects with complex patterns, Long et al. [25] proposed employing the skip architecture, which combined the appearance representation from shallow encoding levels with the high-level representation from deep decoding layers. This allowed for thorough segmentation. This technique applies to biomedical imaging and has shown encouraging results on natural images [25, 26]. Ronneberger et al. [27] and Cui and Liu, [28] developed the U-Net to address the cell tracking issue using skip architecture [29].

We used the U-Net model for segmentation. An up-sampling (decoding) path and a down-sampling (encoding) path make up our network design based on the U-Net. Five convolutional blocks make up the down-sampling pipeline. Each block consists of two convolutional layers with filter sizes of 3*3, 1 stride in each direction, and rectifier activation, increasing the number of feature mappings from 1 to 1024.

Except for the last block, max pooling with stride 2*2 is performed after each block for the down-sampling, reducing feature map size from 240 × 240 to 15 * 15. Every block begins the up-sampling route with a deconvolutional layer. It decreases the number of feature maps by two while increasing the size of feature maps in both directions, increasing the size of feature maps from 15*15 to 240*240. In each up-sampling block, two convolutional layers reduce the total number of feature maps that are generated when the deconvolutional feature maps and the feature maps from the encoding path are concatenated. Unlike the original U-Net design, we use zero padding to preserve the output dimension for all the convolutional layers of the down- and up-sampling routes [29]. To minimize the number of feature maps that represent the foreground and background segmentation, respectively, to two, a 1*1 convolutional layer is utilized. In the network, no ultimately linked layer is activated.

2.7. Setup in the environment of a deep convolutional neural network (DCNN)

We did numerous parameter tunings that range from 2 to 10 hidden layers to obtain the best outcome based on the optimal hidden layer demonstrated in testing. We favor utilizing 12 neurons in a fully linked layer as the number of neurons inside the hidden layer. Each layer's output is calculated using the input parameter, weight, bias, and activation function. We employ the ReLU activation function for the convolutional layer and the Softmax for the output layer to obtain results for categorical data. This work uses root mean square propagation (RMSProp) to help the optimizer understand where the optimization should be made inside the DCNN [30].

Therefore, we utilize the default batch size, which is 32, to decide the number of observations that may be performed before weight altering based on computer configuration and specification for the period or quantity of iterations of the learning process. Until our models converge, the more epochs, the higher the learning outcomes. Fifty epochs were utilized in this investigation.

3. Results and Discussions

We highlight the benefits of the suggested ResNet approach in this section. First, we look at two methods in Experiment 1 that use the output probability maps from ResNet-50 and ResNet-101 to forecast the ultimate lesions from BTs. In the second experiment, we look at the suggested deep learning method's segmentation performance using just one model—U-Net. The following sections provide a description of each experiment's specifics and findings.

3.1. Experiment 1: Multi-class classification

We evaluated the suggested multi-class classification system's effectiveness on a deep neural network in the first experiment. We first used a pre-trained model for training ResNet-50 and ResNet-101 using only MRI images. The experimental outcomes are shown in Tables 6 and 7. Various plots and predicted output results are shown from Figures 4 to 7.

Table 6. Table for loss vs. accuracy

Model	Loss	Accuracy
ResNet-50	0.0330	99.01
ResNet-101	0.0205	99.05

Table 7. Performance metrics for various brain tumors

ResNet 50 model				
Type of tumor	Recall	Precision	Support	F1-score
Glioma	0.97	1.00	300	0.984
Meningioma	0.99	0.98	306	0.984
Pituitary	1.00	0.98	300	0.989
No tumor	1.00	1.00	405	1.00
ResNet 101 model				
Glioma	0.97	1.00	300	0.984
Meningioma	0.97	0.98	306	0.974
Pituitary	0.99	0.97	300	0.979
No tumor	1.00	0.99	405	1.00

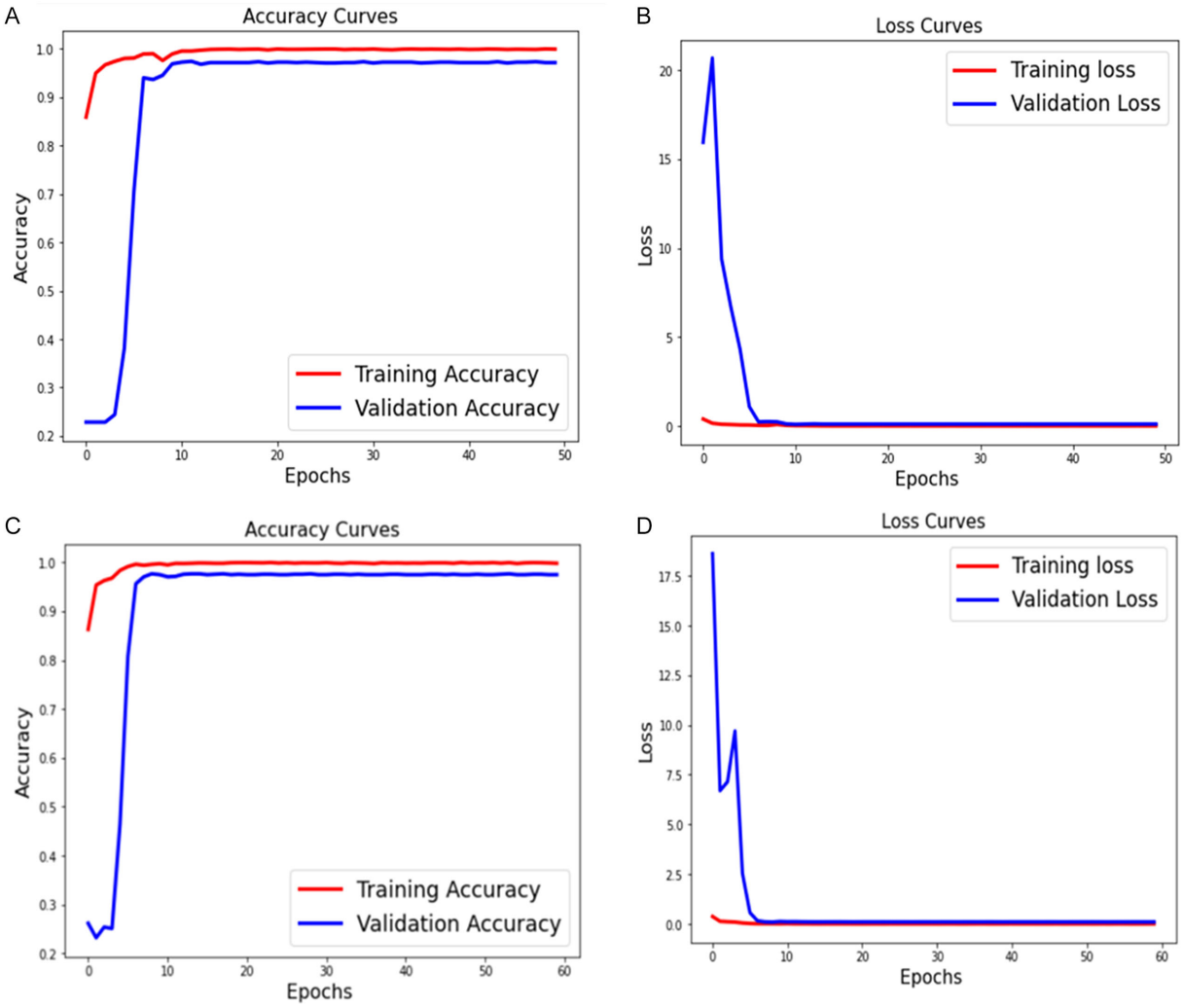

Figure 4. (A) Accuracy plot for ResNet-50, (B) loss plot for ResNet-50, (C) accuracy plot for ResNet-101, and (D) loss plot for ResNet-101

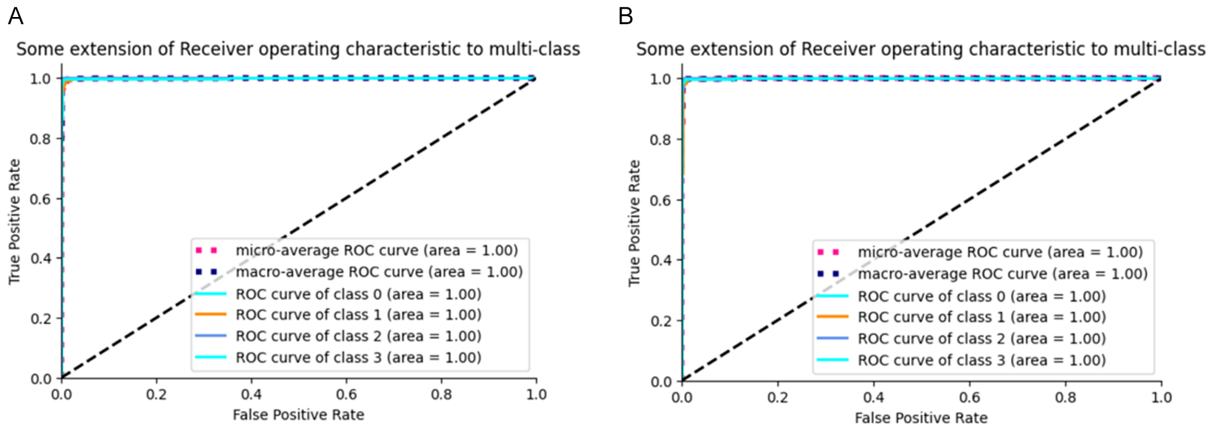

Figure 5. (A) AUC-ROC plot for all classes with ResNet 50 and (B) AUC ROC plot for all classes with ResNet 101

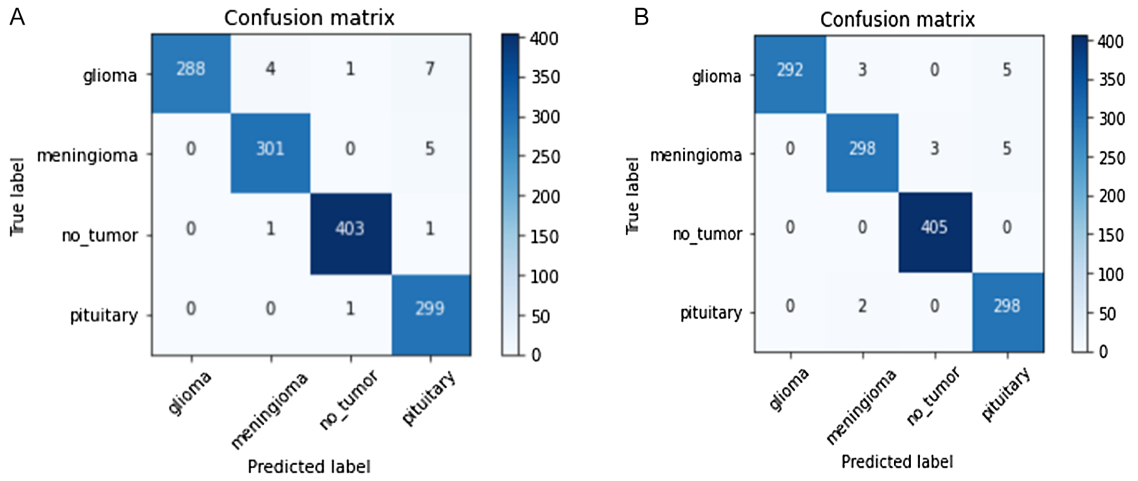

Figure 6. (A) ResNet-50' confusion matrix and (B) ResNet-101' confusion matrix

Figure 7. (A) Prediction output for ResNet-50 and (B) Prediction output for ResNet-101

3.2. Experiment 2: Tumor proportion estimation

We developed U-Net-based fully convolutional networks in this study to address the brain lesion segmentation problem. In essence, semantic segmentation is the task that deals with tumor identification and segmentation. In contrast to earlier studies on this issue that used deep learning, we used a thorough data augmentation scheme that included affine-based deformation or rigid and brightness and elastic distortion-based transformation, which was then coupled with the U-Net that uses the skip-connection architecture [29].

Therefore, a practical segmentation approach should be used on the brain MRI data before categorizing the images into four groups (i.e., NOT tumor, NECROTIC/CORE, EDEMA, ENHANCING). The suggested approach may then use segmented images to identify tumor proportions effectively. Performance analysis is listed in Table 8 below. Various outcomes in this segmentation approach are summarized and presented from Figures 8 to 11.

Table 8. Performance analysis

Performance measures	Values
Loss	0.0179
Accuracy	99.38%
Sensitivity	99.24%
Specificity	99.80%
Dice_Coef	62.02%
Dice_Coef_Necrotic	60.62%
Dice_Coef_Edema	73.38%
Dice_Coef_Enhancing	66.13%
Precision	99.42%
Mean_iou	37.55%

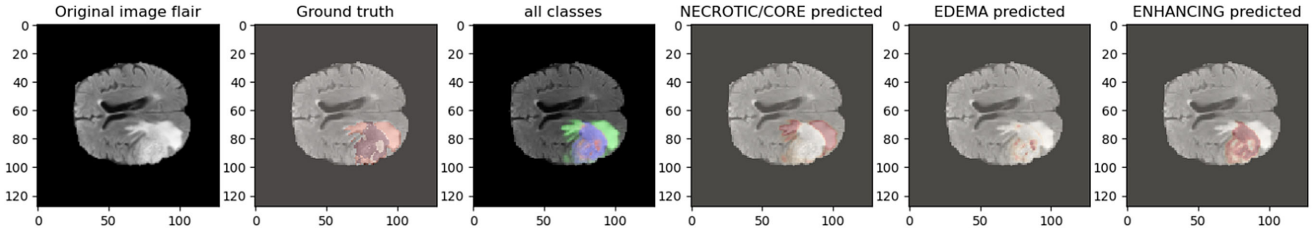

Figure 8. Original scans vs ground truth vs predicted scans

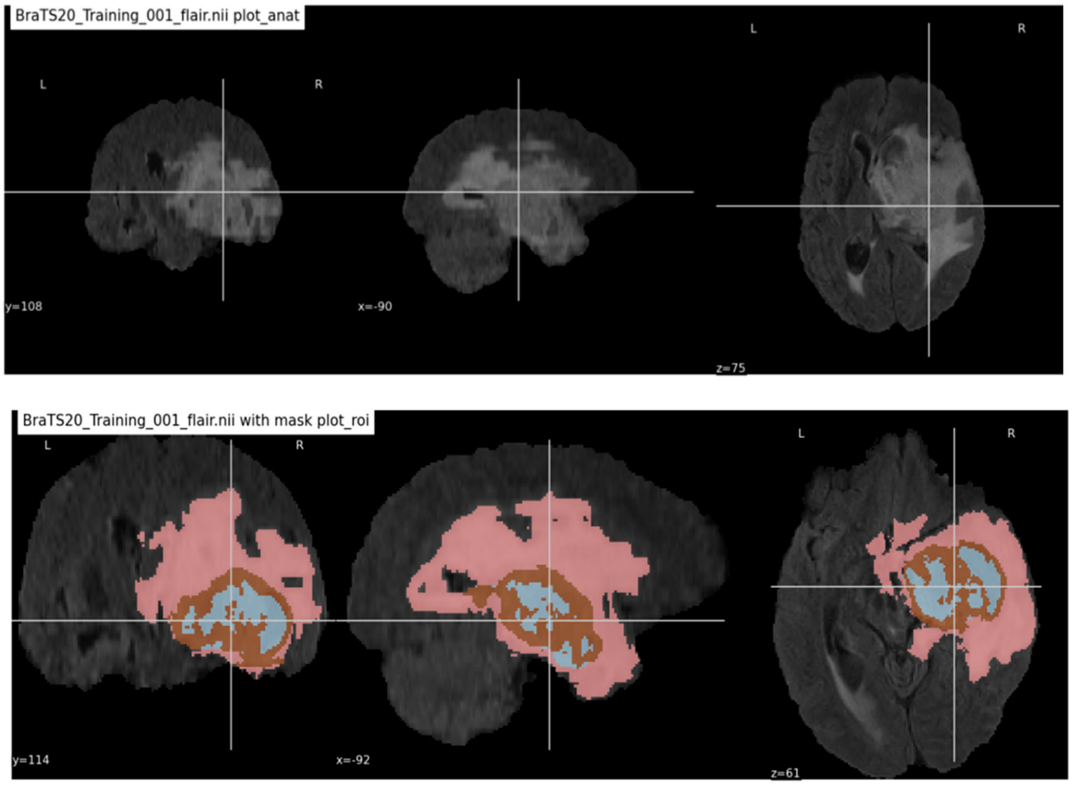

Figure 9. Segments of the tumor using different effects

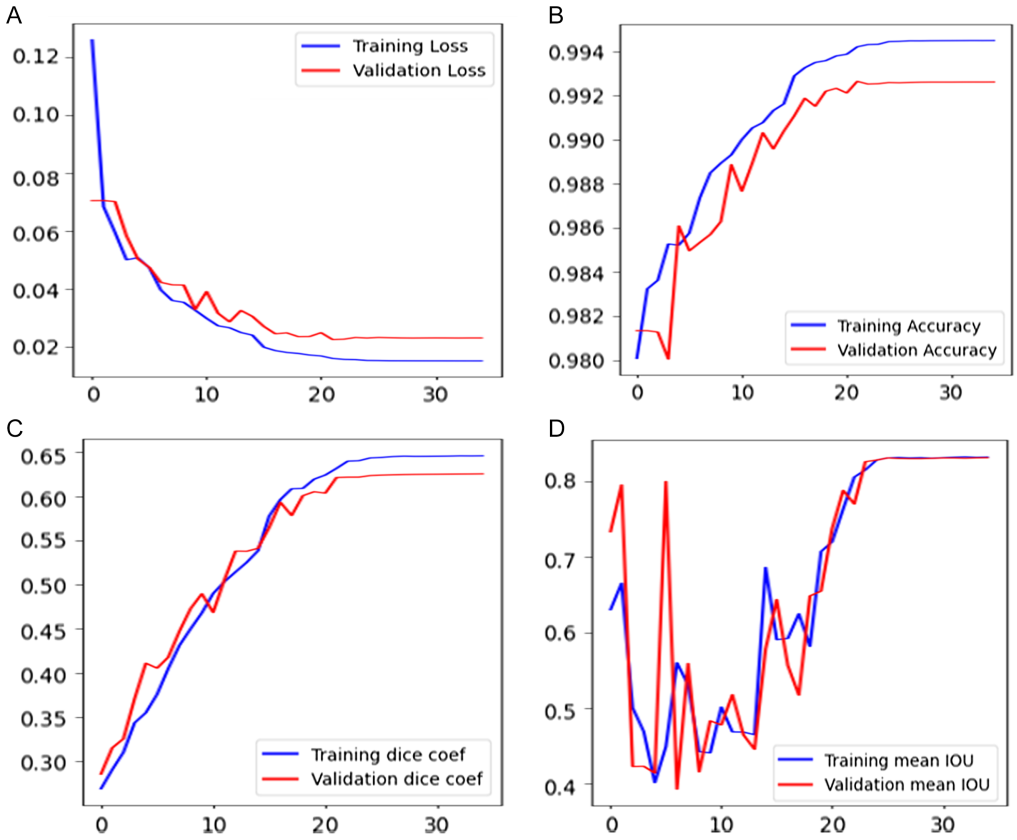

Figure 10. (A) Plot for training and validation accuracy, (B) plot for training and validation loss, (C) plot for dice coefficient, and (D) plot for mean IOU

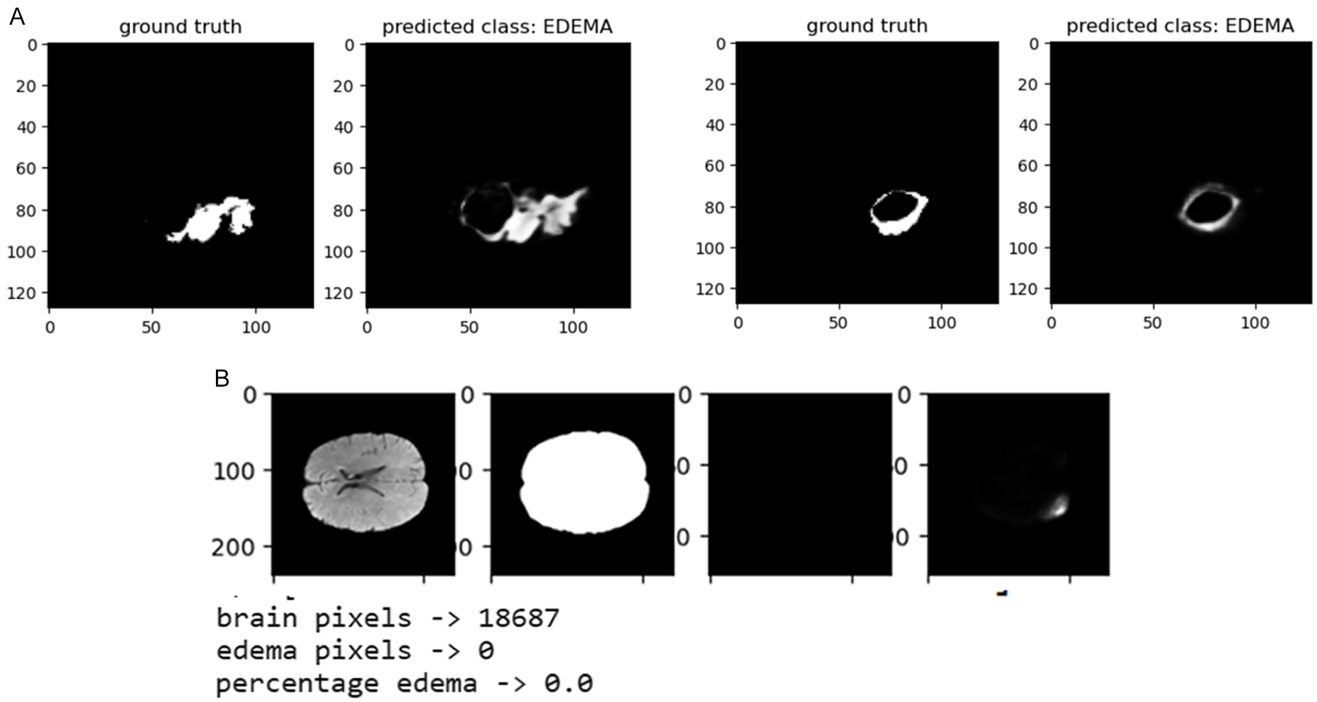

Figure 11. (A) Tumor pixel enhancing output and (B) tumor proportion output

4. Conclusion and Future Directions

Using a dataset of around 9000 images for the training phase, the ResNet approach can classify tumors using MRI scans with a 99.1% and 99.99% accuracy rate. Consistent training data in one class of glioma had an impact on accuracy. With around 500 testing data, the system achieved an accuracy of 99.01% and 99.05%, respectively, for the testing procedure. New data are strongly advised for future studies to improve accuracy and contemporary techniques for data picture preprocessing and data presentation to produce the best data possible.

The proposed ResNet framework was built on top of the ImageNet training. Without altering the fundamental design of the CNN, the ReLU activation function was converted into the softmax activation function. Overall, there were 154 layers instead of 144 after the changes. The recommended model attained the highest-ever classification accuracy of 99.67%. To detect the different BT kinds on the FigShare MRI dataset, we also deployed two deep pre-trained CNN models using the transfer learning approach. The experimental findings showed that the suggested system better distinguished brain malignancies. In addition, the proposed technique calculated more descriptive and discriminative information compared to previous state-of-the-art methods, yielding excellent accuracy.

Additionally, it is clear from testing that the pre-trained CNN model utilizing transfer learning methods generated the best results. However, the proposed framework's accuracy was at its highest level compared to the other pre-trained models. Future research should also explore the 3D dataset using a sizable number of normal brain MRI pictures and a limited number of malignant brain MRI images since the suggested model retrieved more accurate, detailed, and discriminative characteristics along with to draw the volume function as well as the convex hull.

We cannot train a neural network employing the whole 240 × 240 × 155 brain volume due to the computational constraints of using GPUs for state-of-the-art network training. As an alternative, we opted for KAGGLE online notebook.

Conflicts of Interest

The authors declare that they have no conflicts of interest to this work.

Data Availability Statement

The data that support this work are available upon reasonable request to the corresponding author. The dataset analyzed for another part of the study can be found in the BraTS 2020.

References

[1] Zhao, L., & Jia, K. (2016). Multiscale CNNs for brain tumor segmentation and diagnosis. *Computational and Mathematical Methods in Medicine*, *2016*, 8356294. https://doi.org/10.1155/2016/8356294

[2] Kao, P. Y., Shailja, S., Jiang, J., Zhang, A., Khan, A., Chen, J. W., & Manjunath, B. S. (2020). Improving patch-based convolutional neural networks for MRI brain tumor segmentation by leveraging location information. *Frontiers in Neuroscience*, *13*, 1449. https://doi.org/10.3389/fnins.2019.01449

[3] Smoll, N. R., Schaller, K., & Gautschi, O. P. (2013). Long-term survival of patients with glioblastoma multiforme (GBM). *Journal of Clinical Neuroscience*, *20*(5), 670–675. https://doi.org/10.1016/j.jocn.2012.05.040

[4] Ramakrishna, R., Hebb, A., Barber, J., Rostomily, R., & Silbergeld, D. (2015). Outcomes in reoperated low-grade gliomas. *Neurosurgery*, *77*(2), 175–184. https://doi.org/10.1227/NEU.0000000000000753

[5] Bauer, S., Wiest, R., Nolte, L. P., & Reyes, M. (2013). A survey of MRI-based medical image analysis for brain tumor studies. *Physics in Medicine & Biology*, *58*(13), R97. https://doi.org/10.1088/0031-9155/58/13/R97

[6] Mazzara, G. P., Velthuizen, R. P., Pearlman, J. L., Greenberg, H. M., & Wagner, H. (2004). Brain tumor target volume determination for radiation treatment planning through automated MRI segmentation. *International Journal of Radiation Oncology, Biology, Physics*, *59*(1), 300–312. https://doi.org/10.1016/j.ijrobp.2004.01.026

[7] Yamahara, T., Numa, Y., Oishi, T., Kawaguchi, T., Seno, T., Asai, A., & Kawamoto, K. (2010). Morphological and flow cytometric analysis of cell infiltration in glioblastoma: A comparison of autopsy brain and neuroimaging. *Brain Tumor Pathology*, *27*, 81–87. https://doi.org/10.1007/s10014-010-0275-7

[8] Jones, T. L., Byrnes, T. J., Yang, G., Howe, F. A., Bell, B. A., & Barrick, T. R. (2015). Brain tumor classification using the diffusion tensor image segmentation (D-SEG) technique. *Neuro-Oncology*, *17*(3), 466–476. https://doi.org/10.1093/neuonc/nou159

[9] Soltaninejad, M., Yang, G., Lambrou, T., Allinson, N., Jones, T. L., Barrick, T. R., . . . , & Ye, X. (2017). Automated brain tumour detection and segmentation using superpixel-based extremely randomized trees in FLAIR MRI. *International Journal of Computer Assisted Radiology and Surgery*, *12*, 183–203. https://doi.org/10.1007/s11548-016-1483-3

[10] Götz, M., Weber, C., Blöcher, J., Stieltjes, B., Meiner, H. P., & Maier-Hein, K. H. (2014). Extremely randomized trees based brain tumor segmentation. In *MICCAI Workshop: Brain Tumor Segmentation*. https://doi.org/10.5281/zenodo.3666272

[11] Jafari, M., & Kasaei, S. (2011). Automatic brain tissue detection in MRI images using seeded region growing segmentation and neural network classification. *Australian Journal of Basic and Applied Sciences*, *5*(8), 1066–1079. http://www.ajbasweb.com/old/ajbas/2011/August-2011/1066-1079.pdf

[12] Pinto, A., Pereira, S., Correia, H., Oliveira, J., Rasteiro, D. M. L. D., & Silva, C. A. (2015). Brain tumour segmentation based on extremely randomized forest with high-level features. In *37th Annual International Conference of the IEEE Engineering in Medicine and Biology Society*, 3037–3040. https://doi.org/10.1109/EMBC.2015.7319032

[13] Subbanna, N., Precup, D., & Arbel, T. (2014). Iterative multilevel MRF leveraging context and voxel information for brain tumour segmentation in MRI. In *IEEE Conference on Computer Vision and Pattern Recognition*, 400–405. https://doi.org/10.1109/CVPR.2014.58

[14] Wu, W., Chen, A. Y. C., Zhao, L., & Corso, J. J. (2014). Brain tumor detection and segmentation in a CRF (conditional random fields) framework with pixel-pairwise affinity and superpixel-level features. *International Journal of Computer Assisted Radiology and Surgery*, *9*, 241–253. https://doi.org/10.1007/s11548-013-0922-7

[15] Mei, P. A., de Carvalho Carneiro, C., Fraser, S. J., Min, L. L., & Reis, F. (2015). Analysis of neoplastic lesions in magnetic resonance imaging using self-organizing maps. *Journal of the Neurological Sciences*, *359*(1–2), 78–83. https://doi.org/10.1016/j.jns.2015.10.032

[16] Rajendran, A., & Dhanasekaran, R. (2012). Fuzzy clustering and deformable model for tumor segmentation on MRI brain image: A combined approach. *Procedia Engineering*, *30*, 327–333. https://doi.org/10.1016/j.proeng.2012.01.868

[17] Szilágyi, L., Lefkovits, L., & Benyó, B. (2015). Automatic brain tumor segmentation in multispectral MRI volumes using a fuzzy c-means cascade algorithm. In *12th International Conference on Fuzzy Systems and Knowledge Discovery*, 285–291. https://doi.org/10.1109/FSKD.2015.7381955

[18] Menze, B. H., Jakab, A., Bauer, S., Kalpathy-Cramer, J., Farahani, K., Kirby, J., . . . , & van Leemput, K. (2014). The multimodal brain tumor image segmentation benchmark (BRATS). *IEEE Transactions on Medical Imaging*, *34*(10), 1993–2024. https://doi.org/10.1109/TMI.2014.2377694

[19] Havaei, M., Davy, A., Warde-Farley, D., Biard, A., Courville, A., Bengio, Y., . . . , & Larochelle, H. (2017). Brain tumor segmentation with deep neural networks. *Medical Image Analysis*, *35*, 18–31. https://doi.org/10.1016/j.media.2016.05.004

[20] Kamnitsas, K., Ledig, C., Newcombe, V. F. J., Simpson, J. P., Kane, A. D., Menon, D. K., . . . , & Glocker, B. (2017). Efficient multi-scale 3D CNN with fully connected CRF for accurate brain lesion segmentation. *Medical Image Analysis*, *36*, 61–78. https://doi.org/10.1016/j.media.2016.10.004

[21] Pereira, S., Pinto, A., Alves, V., & Silva, C. A. (2016). Brain tumor segmentation using convolutional neural networks in MRI images. *IEEE Transactions on Medical Imaging*, *35*(5), 1240–1251. https://doi.org/10.1109/TMI.2016.2538465

[22] Sheela, V. K., & Babu, S. S. (2015). Preprocessing technique for brain tumor detection and segmentation. *International Research Journal of Engineering and Technology*, *2*(3), 1208–1212. https://www.irjet.net/archives/V2/i3/Irjet-v2i3179.pdf

[23] Ranjbarzadeh, R., Bagherian Kasgari, A., Jafarzadeh Ghoushchi, S., Anari, S., Naseri, M., & Bendechache, M. (2021). Brain tumor segmentation based on deep learning and an attention mechanism using MRI multi-modalities brain images. *Scientific Reports*, *11*(1), 10930. https://doi.org/10.1038/s41598-021-90428-8

[24] Simard, P. Y., Steinkraus, D., & Platt, J. C. (2003). Best practices for convolutional neural networks applied to visual document analysis. In *Seventh International Conference on Document Analysis and Recognition*, 958–963. https://doi.org/10.1109/ICDAR.2003.1227801

[25] Long, J., Shelhamer, E., & Darrell, T. (2015). Fully convolutional networks for semantic segmentation. In *IEEE Conference on Computer Vision and Pattern Recognition*, 3431–3440. https://doi.ieeecomputersociety.org/10.1109/CVPR.2015.7298965

[26] Igarashi, Y., & Fukui, K. (2011). 3D object recognition based on canonical angles between shape subspaces. In *10th Asian Conference on Computer Vision*, 580–591. https://doi.org/10.1007/978-3-642-19282-1_46

[27] Ronneberger, O., Fischer, P., & Brox, T. (2015). U-Net: Convolutional networks for biomedical image segmentation. In *Proceedings of 18th International Conference on Medical Image Computing and Computer-Assisted Intervention*, 234–241. Springer. https://doi.org/10.1007/978-3-319-24574-4_28

[28] Cui, H., & Liu, G. (2015). How noncoding RNAs contribute to macrophage polarization. In C. M. Greene (Ed.), *MicroRNAs and other non-coding RNAs in inflammation* (pp. 59–84). Springer. https://doi.org/10.1007/978-3-319-13689-9_4

[29] Dong, H., Yang, G., Liu, F., Mo, Y., & Guo, Y. (2017). Automatic brain tumor detection and segmentation using U-Net based fully convolutional networks. In *Medical Image Understanding and Analysis: Proceedings of Annual Conference on Medical Image Understanding and Analysis,* 506–517. https://doi.org/10.1007/978-3-319-60964-5_44

[30] Rahmat, R. F., Pratama, M. F., Purnamawati, S., Faza, S., Lubis, A. R., Al-Khowarizmi, A. K., & Lubis, M. (2022). Astrocytoma, ependymoma, and oligodendroglioma classification with deep convolutional neural network. *IAES International Journal of Artificial Intelligence*, *11*(4), 1306–1313. http://doi.org/10.11591/ijai.v11.i4.pp1306-1313

How to Cite: Joshi, M., & Singh, B. K. (2024). Proportion Estimation and Multi-Class Classification of Abnormal Brain Cells. *Medinformatics*, *1*(2), 79–90. https://doi.org/10.47852/bonviewMEDIN42021685